



State-of-charge and state-of-health estimation for lithium-ion batteries based on dynamic impedance technique



Min-Hsuan Hung^a, Chang-Hua Lin^{a,*}, Liang-Cheng Lee^b, Chien-Ming Wang^c

^a Dept. of Electrical Engineering, Tatung University, No. 40, Sec. 3, Zhongshan N. Rd., Taipei City 104, Taiwan, ROC

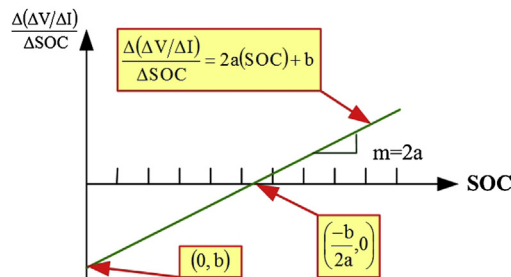
^b Dept. of C. & C. Engineering, St. John's University of S. & T., No. 499, Sec. 4, Danjin Rd., Tamsui Dist., New Taipei City 251, Taiwan, ROC

^c Dept. of Electrical Engineering, National Ilan University, No. 1, Sec. 1, Shen-Lung Rd., I-Lan 260, Taiwan, ROC

HIGHLIGHTS

- This study proposes dynamic impedance to estimate SOC of Li-ion batteries.
- This study proposes projection method to estimate the SOH of Li-ion batteries.
- We developed a real-time SOC and SOH estimation system, combining a MCU with a BMS.

GRAPHICAL ABSTRACT



ARTICLE INFO

Article history:

Received 8 February 2014

Received in revised form

16 May 2014

Accepted 16 June 2014

Available online 7 July 2014

Keywords:

State-of-charge (SOC)

State-of-health (SOH)

Lithium-ion batteries

Battery management system (BMS)

Real-time estimation

ABSTRACT

This study proposes a dynamic impedance method to estimate the state of charge (SOC) and a projection method to estimate the state of health (SOH) of lithium-ion batteries. We defined changes in voltage over changes in current during charging and discharging processes as the dynamic impedance, which was then used to calculate SOC. The proposed methods do not require initial values, and dynamic impedance provides a more accurate reflection of the electrical characteristics of batteries compared to conventional estimation methods. This approach also enables calculations in real-time. The SOH of batteries degenerates with age, which also alters the characteristics of dynamic impedance. The proposed projection method determines the SOH according to the rate of change in dynamic impedance with respect to the SOC. We also developed a real-time SOC and SOH estimation system, combining a microcontroller and estimation methods with a battery management system (BMS). The BMS retrieves the data required for SOC and SOH estimation and includes various protection mechanisms designed to extend the lifespan of the battery. The hardware structure and the software procedure of the developed system are described in detail. We also present the results of experiments verifying the accuracy and feasibility of the proposed estimation methods.

© 2014 Elsevier B.V. All rights reserved.

1. Introduction

Environmental pollution and oil shortages around the world have increased the popularity of electric vehicles [1–5]. Many

nations and major automobile manufacturers are thus investing in the research, development, and promotion of electric and hybrid vehicles. However, high costs have prevented these vehicles from securing a significant share of the market. Battery modules account for a substantial proportion of the overall as well as the core component of electric vehicles. The capacity of these components determines the endurance of the vehicle, while characteristics such

* Corresponding author.

E-mail address: lin@ttu.edu.tw (C.-H. Lin).

as instantaneous discharge current, maximum continuous discharge current, weight, volume, and energy density determine the vehicle's performance [6–10]. Thus, a high-quality battery module is essential for hybrid and electric vehicles to compete with gasoline vehicles.

At present, the battery modules used in electric cars actually comprise hundreds of cells linked in series and parallel. Despite careful screening, the characteristics of individual cells can change during use, which can result in damage to the overall battery module. To extend the life span of battery modules, most battery modules are now equipped with battery management systems (BMSs) [11–14]. The benefits of these devices generally outweigh the additional costs. The primary function of a BMS is to monitor parameters such as the voltage, current, and temperature of the cells in the battery module as well as its overall functioning as a whole, thereby ensuring the safety of its operation. A full-featured BMS provides protective functions which initiate protective measures in the event of abnormalities, such as abnormal voltages, discharge current, or temperatures.

Batteries have limited storage capacity, and are able to transfer energy only within range of their capacity. A battery that is constantly in an overcharged or deeply discharged state is likely to suffer permanent damage. Estimating the state of charge (SOC) is therefore a crucial issue preventing overcharge and over-discharge [15–18]. The SOC can generally be defined as the ratio between the available capacity and maximum available capacity, usually expressed as a percentage [19]. The SOC cannot be derived directly from measuring battery parameters but rather is estimated using algorithms and measurement data. The existing methods of SOC estimation can be broadly divided into online and offline approaches [20–27]. No input of data is required to initiate online methods; rather, parameters are continuously measured during the estimation process. In contrast, offline methods require manual input into the requisite algorithm, commonly involving look-up tables and discharge tests. Offline methods allow for direct comparisons with the default data and are easy to implement; however, they tend to be less accurate, require more time for estimation, and are easily affected by factors associated with the battery, operating conditions, and the environment. As a result, online approaches are the preferred method of SOC estimation. The most recognized methods include the open circuit voltage method and the Coulomb counting method. The former determines the SOC directly, according to the terminal voltage of the battery, while the latter involves integrating the current in time to calculate the energy entering and leaving the battery. Although these methods are simple and inexpensive, they have definite limitations. For instance, the open circuit voltage method uses the terminal voltage to determine the charge capacity, which requires that the battery remain unused for a long period of time. The batteries of electric vehicles are often in constant use, such that the intervals between use are too short to enable accurate SOC estimation [28,29]. The Coulomb counting method calculates only the energy passing in and out of the battery and thus only the changes in the SOC. Determining the actual SOC requires an accurate initial value. As a result, this approach is generally used in conjunction with the open circuit voltage method; however, discrepancies between the initial value and the actual SOC can lead to errors in subsequent results [30,31]. Thus, an increasing number of researchers have been looking for an SOC estimation approach that is more efficient, more rapid, and more accurate. Theories and technologies from other domains, such as artificial neural networks, fuzzy logic, and the Kalman filter, have been applied to online SOC estimation; however, persistent limitations have thus far prevented their being applied commercially. For example, artificial neural networks can be applied to all types of batteries; however, the algorithm requires

a substantial amount of data for training and is slow to converge. Fuzzy logic is also applicable to all types of batteries, but the definitions of its membership functions are extremely subjective and thus unsuitable for large models. Similarly applicable to all types of batteries, the Kalman filter is suitable for dynamic applications such as electric vehicles; however, this algorithm is unduly complex.

Another important parameter of batteries is the state of health (SOH) [32,33]. This represents the extent of aging in the battery and is generally defined as the ratio between the maximum available capacity and the rated capacity, also expressed as a percentage. The calculation of SOH is crucial to understanding the exact aging conditions and maximum available capacity in a battery, as well as a key factor in determining when a battery should be replaced. Conventional techniques include the standard charge and discharge method and the internal resistance method. The former involves discharging the battery to the cut-off voltage using the standard discharge current and then charging the battery to the charge limit voltage using the standard charge current. The ratio between the charge capacity and the rated capacity is then calculated and converted to a percentage which is defined as SOH [34]. In the latter, an unused battery is discharged using a pulse current, during which variations in voltage are recorded. The open circuit voltage, voltage variations, and currents are used to calculate the internal resistance of the battery, which is then used to determine the extent of aging in the battery. Unfortunately, both of these methods have shortcomings. The standard charge and discharge method requires an extremely long period of time to complete measurements, thereby ruling out real-time detection. Furthermore, the measurement process results in the wasteful consumption of a considerable amount of energy and necessitates specialized instruments and equipment that cannot be operated without training. The internal resistance method requires a test component or circuit comprising high resolution equipment to ensure accurate measurement, which makes this method both cumbersome and costly. In addition, the method is applicable only to unused batteries, which again prevents real-time measurement [35,36].

Besides, in order to realize the electrochemical impedance characteristic of the battery, the electrochemical impedance spectroscopy (EIS) was widely applied in several researches [37–40]. The EIS is a nondestructive technique designed to understand the electrochemical impedance characteristic of a battery. Before using this method, an equivalent circuit model is essential. Next, it applies a sinusoidal voltage/current signal to the battery and analyzes the current/voltage response respectively at wide range frequencies [37,40]. And then the electrochemical impedance characteristic of the battery can be determined by some figures, which are plotted by the measured results, for example, Lissajous figure and Nyquist plot [37–40]. However, the used equivalent circuit model must have high accuracy, that is, the equivalent circuit model is complex with a large number of elements. Moreover, EIS cannot be used in the charging or discharging process since it has to apply the various sinusoidal voltage/current signals to the battery and observe the responses. As a result, EIS cannot be used to implement the real-time SOC and SOH estimation function of a battery. Therefore, this study proposed the dynamic impedance method to overcome these mentioned shortcomings.

This study implemented a real-time SOC and SOH estimation system in which BMS is used to capture the electronic characteristics of the battery module. A microcontroller (MCU) serves as the control center of the system to calculate the SOC and SOH of the battery. Chapter 2 details the proposed SOC and SOH estimation methods and Chapter 3 presents the hardware. Chapter 4 describes the software procedures, and Chapter 5 presents experiment results verifying the efficacy of the proposed techniques.

2. Proposed battery SOC and SOH estimation methods

As previously mentioned, the common limitations of existing SOC estimation methods include 1) the need for initial values or historical data, 2) the inability to perform real-time detection, and 3) the inability to determine the actual SOC from calculations in the event of fluctuations in SOH. Current SOH estimation methods are limited by: 1) the inability to perform real-time detection and 2) the necessity of additional test components or circuits. To overcome these issues, this study proposed a dynamic impedance method to estimate the SOC and a projection method to estimate the SOH of batteries. Neither of these methods includes temperature as a parameter in this study.

For the dynamic impedance method, we define the ratio of the voltage and current variations (ΔV , ΔI) of a battery during the charging and discharging processes as the dynamic impedance. This serves as the basis for SOC estimation, obviating the need for initial values or historical data. The proposed method is able to produce results very rapidly (approximately 10 s), making it applicable to near real-time measurement. The proposed projection method does not require additional testing components or circuits, using the results of dynamic impedance to calculate the SOH of the battery. Most importantly, the parameters used in the proposed methods are continuously updated according to the SOH of the battery throughout calculation process, thereby providing a true indication of the SOC of the battery. In this chapter, we present the theory and parameter calculations of the two proposed methods.

2.1. Theory of dynamic impedance method and projection method

For SOC estimation, this study employed voltage and current variations ΔV and ΔI captured by the BMS from the battery module (comprising 8 cells) under specific load conditions at a sampling rate of 1 Hz as shown in Fig. 1.

$$\Delta V = |V_2 - V_1| \quad (1)$$

$$\Delta I = |I_2 - I_1| \quad (2)$$

The ratio of the two is defined as the dynamic impedance:

$$\frac{\Delta V}{\Delta I} = \frac{|V_2 - V_1|}{|I_2 - I_1|} \quad (3)$$

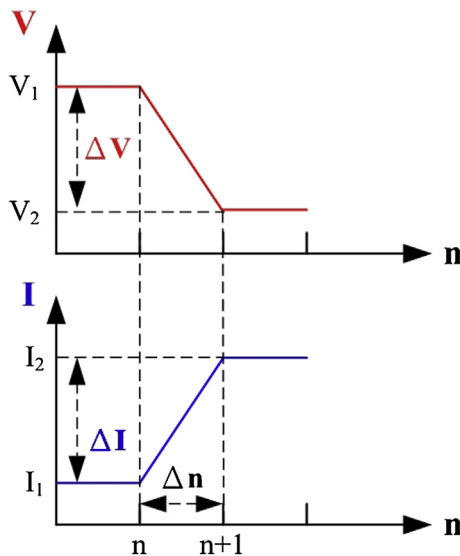


Fig. 1. Dynamic impedance ($\Delta V/\Delta I$).

This study tested a lithium-ion battery module to determine the relationship between SOC and dynamic impedance. We monitored the voltage and current values while a battery tester discharged the battery from an SOC of 100% to that of 0%; the results of which are presented in Fig. 2. The curve in the figure is similar to a parabolic curve. Dynamic impedance can therefore be expressed as

$$\frac{\Delta V}{\Delta I} = a(\text{SOC})^2 + b(\text{SOC}) + C. \quad (4)$$

The parameters a , b , and c reflect the electrical characteristics of the lithium-ion battery. Eq. (4) can be rewritten as follows:

$$\frac{\Delta V}{\Delta I} = a \left(\text{SOC} + \frac{b}{2a} \right)^2 + \left(\frac{4ac - b^2}{4a} \right). \quad (5)$$

From the above equation we can see that the minimum value of the curve is $(-b/2a, 4ac - b^2/4a)$ and the curvature of the parabola is a . This latter value determines the orientation of the parabola (upward if a is positive and downward if a is negative). Larger values for a indicate a greater curvature; dynamic impedance is therefore greater when the battery is closer to empty or fully charged. Experimental results revealed that under the same load conditions, older batteries display greater variations in voltage (ΔV) when they are near empty or full. In other words, the dynamic impedance is greater. From this, we can infer that the dynamic impedance of aged batteries is greater than that of new batteries when they are near empty or full. This enables us to determine the SOH of the battery according to parameter a . In terms of SOC, Eq. (4) shows that one dynamic impedance value corresponds to two different SOC values. Therefore, we cannot merely use the dynamic impedance for the estimation of SOC. To overcome this problem, we further calculated the derivative in SOC with respect to the nonlinear dynamic impedance in order to obtain a single solution for the SOC. A linear equation using one variable can be derived using Eq. (4), thereby providing a single solution for SOC.

$$\frac{\Delta(\Delta V/\Delta I)}{\Delta \text{SOC}} = 2a(\text{SOC}) + b \quad (6)$$

Using Eq. (6), we can plot the relationship between $\Delta(\Delta V/\Delta I)/\Delta \text{SOC}$ and SOC, as shown in Fig. 3. The graph shows that the equation is an injection, such that when $\Delta(\Delta V/\Delta I)/\Delta \text{SOC}$ is obtained, the corresponding SOC of the battery can also be derived. When $\Delta(\Delta V/\Delta I)/\Delta \text{SOC}$ is 0, SOC is $-(b/2a)$. We can therefore rewrite Eq. (6) as follows:

$$\text{SOC} = \left[\frac{\Delta(\Delta V/\Delta I)}{\Delta \text{SOC}} - b \right] / 2a \quad (7)$$

Eq. (7) provides the only solution for the SOC. In the next section, we examine the relationship between parameters a and b in

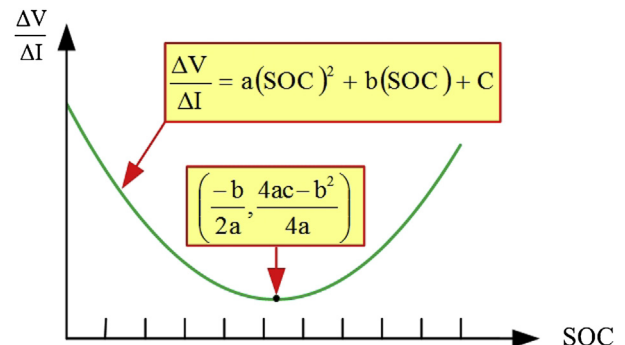
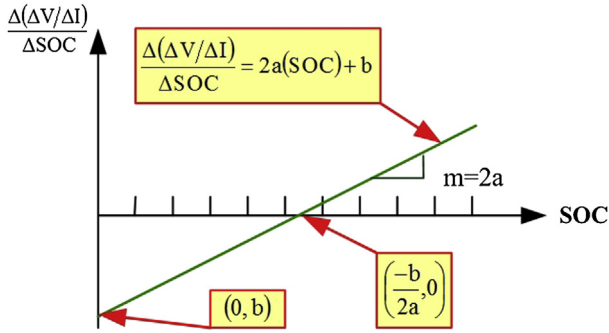


Fig. 2. Characteristic curve of SOC corresponding to dynamic impedance.

Fig. 3. Relationship between $\Delta(\Delta V/\Delta I)/\Delta SOC$ and SOC.

detail. $\Delta(\Delta V/\Delta I)$ can be obtained for real-time operations while the battery is being charged or discharged. However, $\Delta SOC = SOC_2 - SOC_1$, which is unknown. In the event that the load conditions of the batteries change, the relationship between the load current and time is linear. As a result, the relationship between the current and the SOC is as shown in Fig. 4.

The above figure illustrates that ΔSOC can be derived using the Coulomb counting method:

$$\begin{aligned} \Delta SOC &= |SOC_2 - SOC_1| = \frac{1/2 \times |I_2 + I_1| \times [(n+1) - n]}{Q_{rated}} \\ &= \frac{1}{2} \times \frac{|I_2 + I_1| \times \Delta n}{Q_{rated}} = \frac{1}{2} \times \frac{|I_2 + I_1| \times \Delta n}{C_{rated} \times 3600} \end{aligned} \quad (8)$$

where the frequency of data acquisition in the BMS is 1 Hz. Thus, $\Delta n = 1$ s. The term $C_{rated} \times 3600$ (rated current multiplied by one hour) represents the rated capacity of the battery cell.

Fig. 2 indicates that the dynamic impedance of the battery changes with the SOC. We can thus infer that under conditions of severe aging, the voltage increments and decrements of the battery will be more pronounced, with a resulting increase in the dynamic impedance. In other words, the dynamic impedance of an aged battery is far higher than that of a new battery. This is evident in Fig. 5, in which curve A is the characteristic curve of a new battery and curve B is that of an aged battery. Under these conditions, if we calculate the rate of change in the characteristic curve with respect to the SOC, the slope of the SOC variation curve will be greater, as shown in Fig. 6. Thus, the greater the degree of aging in

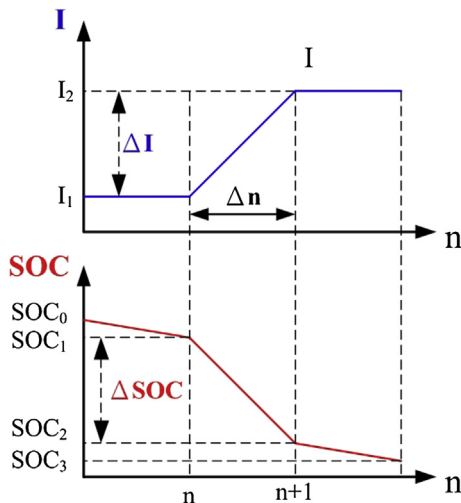
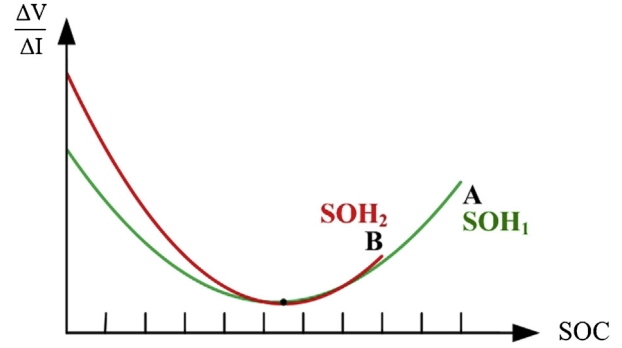


Fig. 4. Load current and SOC waveforms under variations in load.

Fig. 5. $\Delta V/\Delta I$ vs. SOC under various SOH.

the battery, the greater the slope of the $\Delta(\Delta V/\Delta I)/\Delta SOC$ to SOC characteristic curve. In addition, the length of the projection on the SOC axis will be shorter. Curves A (green) and B (red) in Fig. 6 illustrate (in the web version) the SOH corresponding to two degrees of aging. Smaller slopes lead to longer projections on the SOC, which indicate that the battery can store and release a greater amount of energy. In contrast, greater slopes lead to shorter projections on the SOC axis, indicating that the battery is unable to store or release as much energy. Thus, as shown in Fig. 6, calculating the slope of the characteristic curve provides a basis for determining the SOH of the battery. This method is referred to as the projection method.

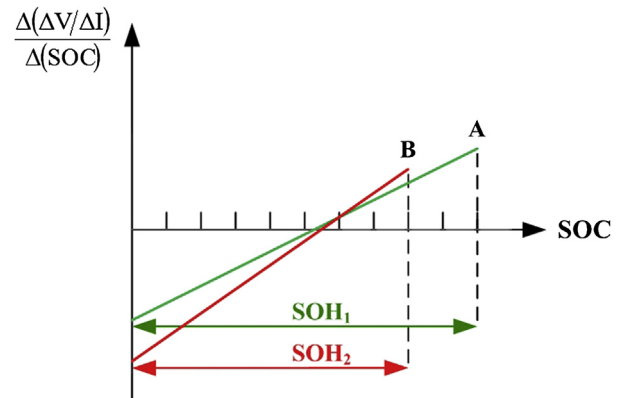
2.2. Parameter calculation for dynamic impedance method and projection method

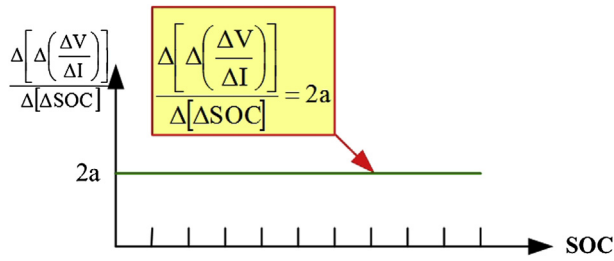
The above discussion indicates that by deriving parameters a and b , we can use Eq. (7) to calculate the SOC of the battery. The steps to deriving parameters a and b are as follows.

2.2.1. Step 1: Obtain parameter a

First, we can use the rate of change in the tangent slope $\Delta(\Delta V/\Delta I)/\Delta SOC$ with respect to the SOC in order to derive the characteristic curve of the relationship between dynamic impedance and the SOC by calculating two tangent slopes, as shown in Fig. 7. As can be seen in the figure, we need only obtain the second derivative of the dynamic impedance with respect to SOC to derive a fixed value: $2a$. The equation can be written as

$$\frac{d^2(\Delta V/\Delta I)}{dSOC} = \frac{\Delta[\Delta(\Delta V/\Delta I)]}{\Delta[SOC]} = 2a \quad (9)$$

Fig. 6. $\Delta(\Delta V/\Delta I)/\Delta SOC$ vs. SOC under various SOH.

Fig. 7. Relationship curve between $\Delta(\Delta V/\Delta I)/\Delta SOC$ and SOC.

However, as shown in Fig. 6, the value of a is influenced by the degree of aging in the battery, and for this reason, a is not fixed but rather updates constantly with the SOH of the battery.

2.2.2. Step 2: Obtain parameter b

Fig. 8 is used to obtain parameters b , SOC and SOH. Lines A and line B are the characteristic curves of a new battery and the current battery, respectively. Their respective linear functions are $y = 2a_1x + b_1$ and $y = 2a_2x + b_2$. Both have length L and parameters a_1 and b_1 are known. Point (x_1, y_1) is the intersection node. The SOH of the new battery is SOH_{origin} and the SOH of the current battery is SOH_{now} . By substituting point (x_1, y_1) into the linear functions, we obtain

$$y_1 = 2a_1x_1 + b_1 \quad (10)$$

and

$$y_1 = 2a_2x_1 + b_2 \quad (11)$$

Adjusting these equations (10) and (11) provides x_1 and y_1

$$x_1 = \frac{-(b_2 - b_1)}{2(a_2 - a_1)} \quad (12)$$

and

$$y_1 = \frac{a_2b_1 - a_1b_2}{a_2 - a_1} \quad (13)$$

These two variables are related via the triangle in Fig. 8, as follows:

$$\frac{x_1 - (-b_2/2a_2)}{x_1} = \frac{y_1}{y_1 - b_2} \quad (14)$$

Substituting equations (12) and (13) for x_1 and y_1 enables us to rewrite equation (14) as

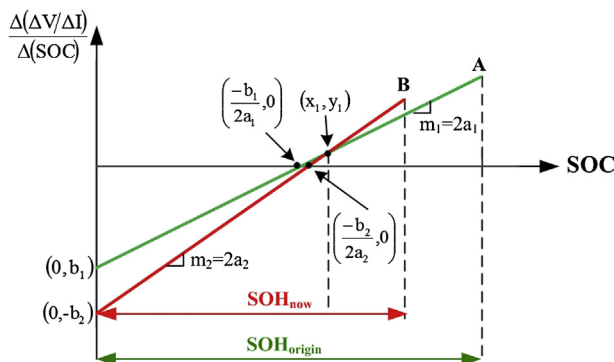


Fig. 8. Diagram outlining parameter calculation.

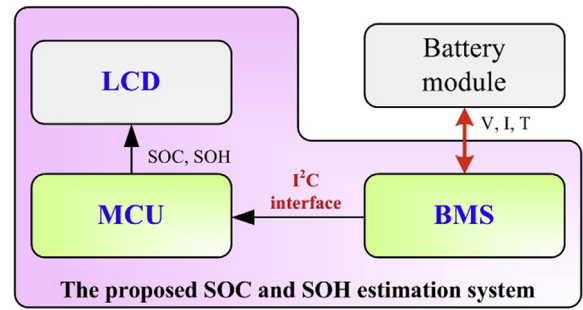


Fig. 9. Proposed SOC and SOH estimation system.

$$\begin{aligned} & \frac{[-(b_2 - b_1)/2(a_2 - a_1)] + (b_2/2a_2)}{[-(b_2 - b_1)/2(a_2 - a_1)]} \\ &= \frac{[(a_2b_1 - a_1b_2)] / \frac{(a_2 - a_1)}{[(a_2b_1 - a_1b_2)/(a_2 - a_1)] - b_2}} \end{aligned} \quad (15)$$

Adjusting this equation gives us b_2 :

$$b_2 = \frac{b_1(a_2 - a_1)}{2a_2} \quad (16)$$

Thus, parameter b_2 is a relationship among a_1 , a_2 and b_1 and is therefore influenced by the SOH of the battery. Furthermore, parameter b_2 is not a constant.

2.2.3. Step 3: Obtain SOC

The SOC is obtained by substituting parameters a and b into Eq. (7).

2.2.4. Step 4: Obtain parameter SOH

According to Fig. 8, the relationship between SOH_{now} and SOH_{origin} can be written as

$$\frac{SOH_{now}}{SOH_{origin}} = \frac{L \times \cos \theta_2}{L \times \cos \theta_1} = \frac{\cos(\tan^{-1} 2a_2)}{\cos(\tan^{-1} 2a_1)} \quad (17)$$

Thus

$$SOH_{now} = SOH_{origin} \times \frac{\cos(\tan^{-1} 2a_2)}{\cos(\tan^{-1} 2a_1)} \quad (18)$$

where the SOH_{origin} is defined as 100%.

The above inferences show that both the SOC and the SOH of batteries are associated with the value of a . Thus, the dynamic impedance method establishes a connection between SOC and SOH.

3. Hardware structure

This study combined an MCU with the BMS in order to implement the SOC and SOH estimation methods presented in the previous chapter. Fig. 9 presents the relevant block diagram. In the proposed system, the BMS directly detects the voltage and current of each cell in the battery module during charging and discharging. It also detects the temperature of the battery module. This data serves as a reference from which to initiate protective mechanisms related to over voltage (OV), under voltage (UV), over current (OC), short circuit (SC), over temperature (OT), and under temperature (UT). Furthermore, the data obtained by the BMS is also sent to the MCU via the I^2C (inter-integrated circuit) interface for further

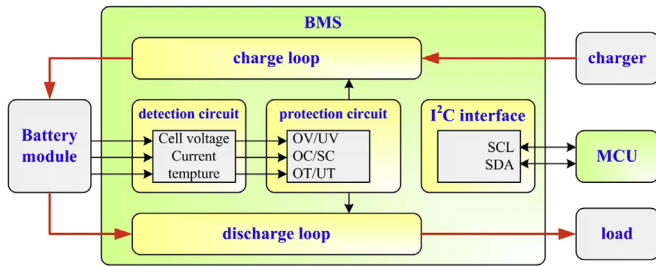


Fig. 10. Battery management system (BMS).

processing. The resulting SOC and SOH are then displayed on an LCD.

3.1. Battery management system (BMS)

This study employed a BMS to monitor the charging and discharging processes and perform protective functions, as outlined in the block diagram in Fig. 10. The BMS in this study was designed for Li-ion batteries and is suitable for high power applications, such as electric bicycles, electric motorcycles, and UPS [41]. The BMS comprises a detection circuit, a protection circuit, an I²C interface, and two independent loops for charging and discharging. The

detection circuit measures the voltage and current of each cell in the battery module during charging and discharging as well as the temperature of the battery module.

Fig. 11 illustrates the voltage and current detection circuit used in this study. The operational principle of the voltage detection circuit adopts the negative electrode of the bottommost battery cell (cell₁) as the negative electrode of the battery module. In other words, this electrode serves as the voltage reference point. By measuring the voltages on the positive electrode of each cell ($V_1 \sim V_N$) and then subtracting the voltage on the positive electrode of the previous cell, we can obtain the voltage of each cell (V_{cN}):

$$V_{cN} = V_N - V_{N-1} \quad (19)$$

BMS can measure the voltage of each cell and the total voltage of the battery module by using this method. The operational principle of the circuit for current detection involves equipping the charging and discharging circuits with a current sampling resistor R_{sense} . When the current flows through R_{sense} , a voltage drop V_{sense} will occur. The BMS retrieves this voltage signal and converts it into a current signal, as follows:

$$I = V_{\text{sense}} / R_{\text{sense}} = V_{\text{sense}} / 0.005 \, \Omega = 200 \, V_{\text{sense}} \quad (20)$$

The R_{sense} used in this study is 0.005 Ω .

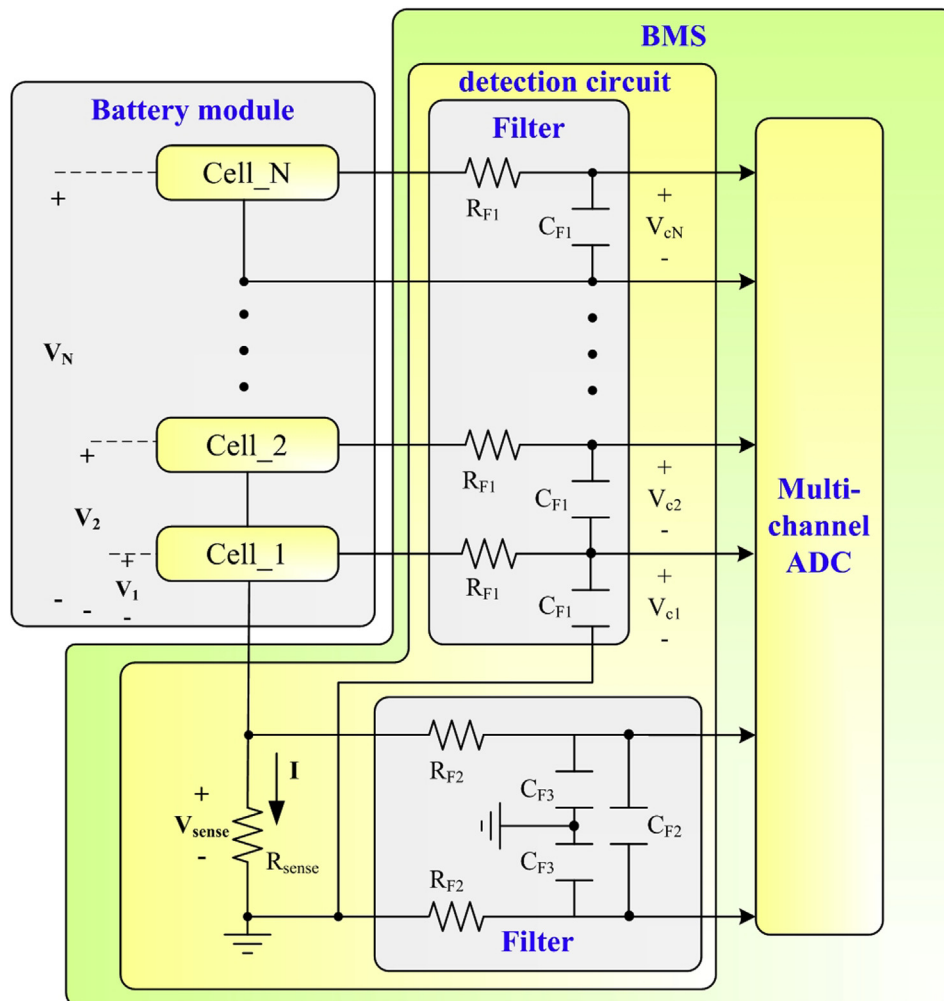


Fig. 11. Detection circuit of BMS.

As shown in Fig. 11, the voltage and current data are sent to multi-channel ADCs for analog-to-digital conversion, the specifications of which are listed in Table 1. The respective ADCs on the current channel and the voltage channel each possess a bits to signify positivity and negativity, such that the actual resolutions are 15 bit and 11 bit. Thus, the current and voltage resolutions are

$$I_{\text{resolution}} = (250 \text{ mV}/0.005 \Omega)/2^{15} = 1.52 \text{ mA} \quad (21)$$

and

$$V_{\text{resolution}} = 5 \text{ V}/2^{11} = 2.44 \text{ mV} \quad (22)$$

The produced signals are weak because the resolution of the ADC in the detection circuits the detection circuits in the BMS operate at the in the BMS operate at the mV level. Therefore, measurement noise may lead to errors in calculation. The following steps were introduced to mitigate this problem.

3.1.1. IC VCC power supply input capacitor and decoupling capacitor

A 10 μF electrolyte capacitor and 0.1 μF ceramics capacitor were used as the input capacitor and decoupling capacitor, respectively. They were placed as close as possible to the VCC pin of the IC and the traces were shortened and widened to minimize low frequency and high frequency coupling noise.

3.1.2. LDO output capacitor

To reduce high frequency noise, the output of the LDO was connected to a 10 μF ceramic capacitor with low ESR (equivalent series resistance, ESR). In addition, the ceramic capacitor was placed as close as possible to the LDO output pin.

3.1.3. Voltage measurement circuit

A low pass filter was used to minimize differential noise and voltage spikes in the voltage measurement circuit. This filter comprised a resistor and capacitor, as shown in Fig. 11, where $R_{F1} = 510 \Omega$ and $C_{F1} = 1 \mu\text{F}$. In consideration of ESD and EMI, according to [42] the voltage sense circuit was shielded using a GND plane from the connector for connecting the battery cell to low pass filter.

3.1.4. Current measurement circuit

The current measurement circuit transmitted current signal through a low pass filter to the pin of the IC. The low pass filter comprised two resistors R_{F2} and two capacitors C_{F2} (filtering differential noise) and a capacitor C_{F3} (filtering common noise), as shown in Fig. 11, where $R_{F2} = 100 \Omega$, $C_{F2} = 0.1 \mu\text{F}$ and $C_{F3} = 0.1 \mu\text{F}$.

3.1.4. GND system

Separating the grounds of analog, digital, and power is a simple, effective method used for noise suppression. This does not imply that the grounds are electrically isolated within the system. They must share a common point, preferably at the negative terminal of the battery module in this study.

Table 1
The specifications of multi-channel ADC.

Current channel	
Resolution	16-Bit (signed)
Input voltage (V_{SENSE}) range	$\pm 250 \text{ mV}$
Voltage channel	
Resolution	12-Bit (signed)
Input voltage (V_{CN}) range	$-0.3 \text{ V} \sim 5.0 \text{ V}$

As the battery module charges and discharges, the BMS continually monitors the condition of the battery module to ensure that the battery is being used under normal (safe) conditions. In the event of abnormal operations, protective mechanisms must be initiated. The BMS in this study possesses comprehensive protective mechanisms divided into two stages. The first stage includes basic protection with regard to over voltage (OV), under voltage (UV), over current (OC), short circuit (SC), over temperature (OT), and under temperature (UT). When the BMS detects voltages, currents, or temperatures reaching a preset threshold, a warning signal notifies the user to replace the battery module. The second stage involves advanced protection for extremely high voltage permanent failure (VHPF), extremely low voltage permanent failure (VLPPF), cell voltage unbalance permanent failure (CUPF), and MOSFET failure permanent failure (MFPF). When the BMS perceives voltages, currents, or temperatures that require second-stage protection, the protection circuit shown in Fig. 12 is initiated. The MOSFET driver turns off the MOSFETs on the charge or discharge loops, thereby preventing the battery module from continuing to charge or discharge.

The data obtained by the BMS is sent to the protection circuit, as well as, the MCU via the I^2C interface for computation, as shown in Fig. 13. The I^2C interface is a communication interface for peripheral devices such as the BMS, the MCU, and the digital-to-analog converter. The interface has only two pins, one for SDA (data) and one for SCL (clock), as shown in Fig. 13. This involves transmitting data through a master-slave relationship, making it very easy to use. A single master controls all of the transmission lines, and the devices at each slave node are given different device addresses, which the master node uses for the selection of slave devices. The slave devices then passively meet the requirements of the master by reading or writing data. However, the SCL is provided by the master, such that interferences in synchronization can occur when the distance between the master and the slave is too great or when severe noise exists in the wiring. In the proposed real-time SOC and SOH estimation system, the master is the MCU, and the slave is the BMS. Thus, the MCU will select the device address of the BMS and then uses the I^2C interface to read the information from the BMS and conduct the required operations.

3.2. Microcontroller (MCU)

The core of the proposed real-time SOC and SOH estimation system is the MCU, which is connected to the BMS via an I^2C interface and retrieves the voltages and currents of each cell in the battery module. Furthermore, it executes the proposed dynamic impedance and projection methods for estimating the SOC and SOH of the battery module before using the input/output (I/O) ports to display the results on the LCD.

The MCU used in this system comprises a processor, an I^2C interface, and five sets of I/O ports (A ~ E), as shown in Fig. 14. The input and output ports are used to transmit analog signals and link to various peripheral devices. For example, the system outputs 11 sets of analog signals to control the LCD and display the required

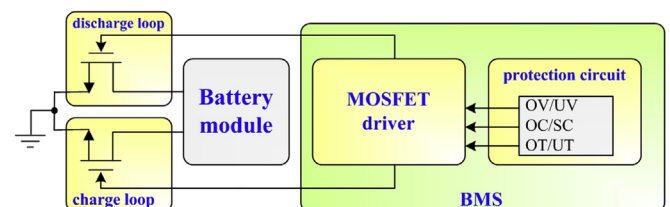
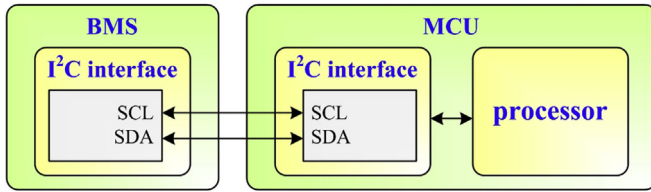


Fig. 12. Protection circuit of BMS.

Fig. 13. I^2C interface of BMS.

text. The 8-bit processor is able to process 16 MIPS (millions of instructions per second), which is sufficient to connect to the BMS, retrieve data, conduct the calculations associated with the dynamic impedance and projection methods, and control the LCD within one second. Thus device also possesses multiple interrupt capability, which enables users to establish various priorities. The frequency of the internal timer reaches 32 kHz, which is sufficient to process the associated programs. The MCU also contains an I^2C interface to set it as the master node, assign device addresses, link it to the slave devices, and access data in the device registers. Once the MCU is connected to the BMS through the I^2C interface, it can access the data in eight cell voltage registers and the current register then excise the calculations.

4. Software procedures of SOC and SOH estimation

In this chapter we outline the software used to implement SOC and SOH estimation using the hardware described above. The BMS captures the data related to voltage and current of the battery modules and sends it to the MCU via the I^2C interface for calculation. Once the dynamic impedance and parameters a_{now} and b_{now} are derived, the current SOC and SOH can be calculated and the information on the LCD renewed. Fig. 14 displays the program procedure.

In Fig. 15, the program used to estimate the SOC and SOH can be divided into a main routine and an interrupt subroutine. When the program begins, the I^2C interface, the LCD, and the I/O port modules are initialized. In accordance with the sampling frequency of the BMS, the timer is set to enter interrupt service after executing one interrupt each second, such that the program is executed repeatedly. Upon entering into the interrupt subroutine, a connection is made with the BMS via the I^2C interface to retrieve data related to voltage and current from each cell. The voltage V of the battery module is then calculated. First, if V equals 0, then the BMS has already initiated the protective functions, and the battery module is

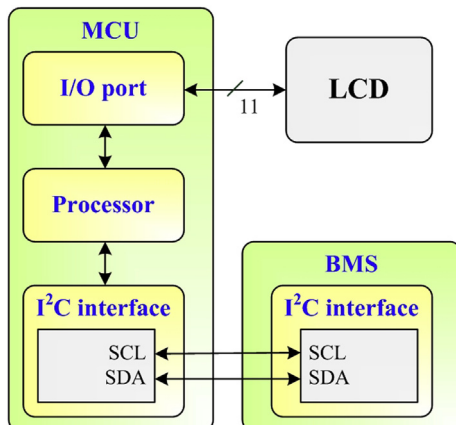


Fig. 14. Microcontroller.

cut-off from charging and discharging. Thus, the program is ended. Next, if current change ΔI is 0, then there is no change in the current, and the interrupt is ended; otherwise, the operations continue. If the voltage change equals 0, the interrupt is ended; if not, then the various parameters, the SOC, and the SOH are calculated as follows.

Step 1: Calculate dynamic impedance $(\Delta V/\Delta I)_n$ based on the latest voltage and current data as well as the previous voltage and current data.

Step 2: To eliminate extreme values, record the results of Step 1 and calculate the average $(\Delta V/\Delta I)_n$ of the three latest dynamic impedance results in order to minimize fluctuations.

Step 3: Record the results of Step 2 and calculate $\Delta(\Delta V/\Delta I)_n$ using the two latest results.

Step 4: Record the results of Step 3 and calculate $\Delta[(\Delta V/\Delta I)_n]_n$ using the two latest results.

Step 5: Record the current data and calculate ΔSOC_n using the Coulomb counting method using the two latest sets of data.

Step 6: Record the results of Step 5 and calculate $\Delta(\Delta SOC_n)_n$ using the two latest results.

Step 7: Substitute the results of Steps 4 and 6 into Eq. (9) to derive parameter a_{now} .

Step 8: Substitute the parameter a_{now} derived in Step 7 into Eq. (16) to obtain parameter b_{now} .

Step 9: Substitute the results of Steps 3 and 5 and parameters a_{now} and b_{now} into Eq. (7) to obtain current SOC.

Step 10: Substitute parameters a_{now} and a_{origin} into Eq. (18) to calculate SOH.

Step 11: Update the results of the SOC, SOH, and parameters a and b and display them on the LCD.

Step 12: End the interrupt and return to the main routine until the timer reaches 1 s, and then re-execute the interrupt.

5. Experiment results

This study used a battery tester (GBT-2636) to verify the proposed SOC and SOH estimation methods. The battery tester allows users to set experiment step, including the amplitude of the discharge current and the duration of the step. We used Samsung ICR18650-22P lithium-ion batteries in a 18650 package. The capacity of each battery cell was 2150 mAh. All relevant specifications are presented in Table 2 [43].

Fig. 16 presents the experimental platform comprising the battery tester, the 8S1P battery module, and the SOC and SOH estimation system. The 8S1P battery module was used in the all verification experiments in this study. Ambient temperature was maintained between 24 and 25 °C. This platform was used to verify the proposed dynamic impedance and projection methods. We first mapped out the discharge sequences for the battery tester, setting the discharge current amplitudes and duration of each sequence. The battery tester then discharged the battery module until the battery ran out and the voltage of the battery module decreased to the cut-off voltage. During the experiment, the battery tester recorded the voltage, discharge current, and discharge energy. We analyzed the data to obtain ΔV , ΔI , and the dynamic impedance, plotting the corresponding graphs to observe the trends and verify the accuracy of the proposed estimation methods.

To verify the accuracy of the proposed estimation methods, we first used the battery tester to establish an experiment procedure comprising eight sequences, as shown in Table 3. We adopted three different currents for use during the experiment: 2.15 A (1 C), 4.3 A (2 C), and 8.6 A (4 C). This procedure was repeated such that the battery module discharged continuously until exhaustion, while

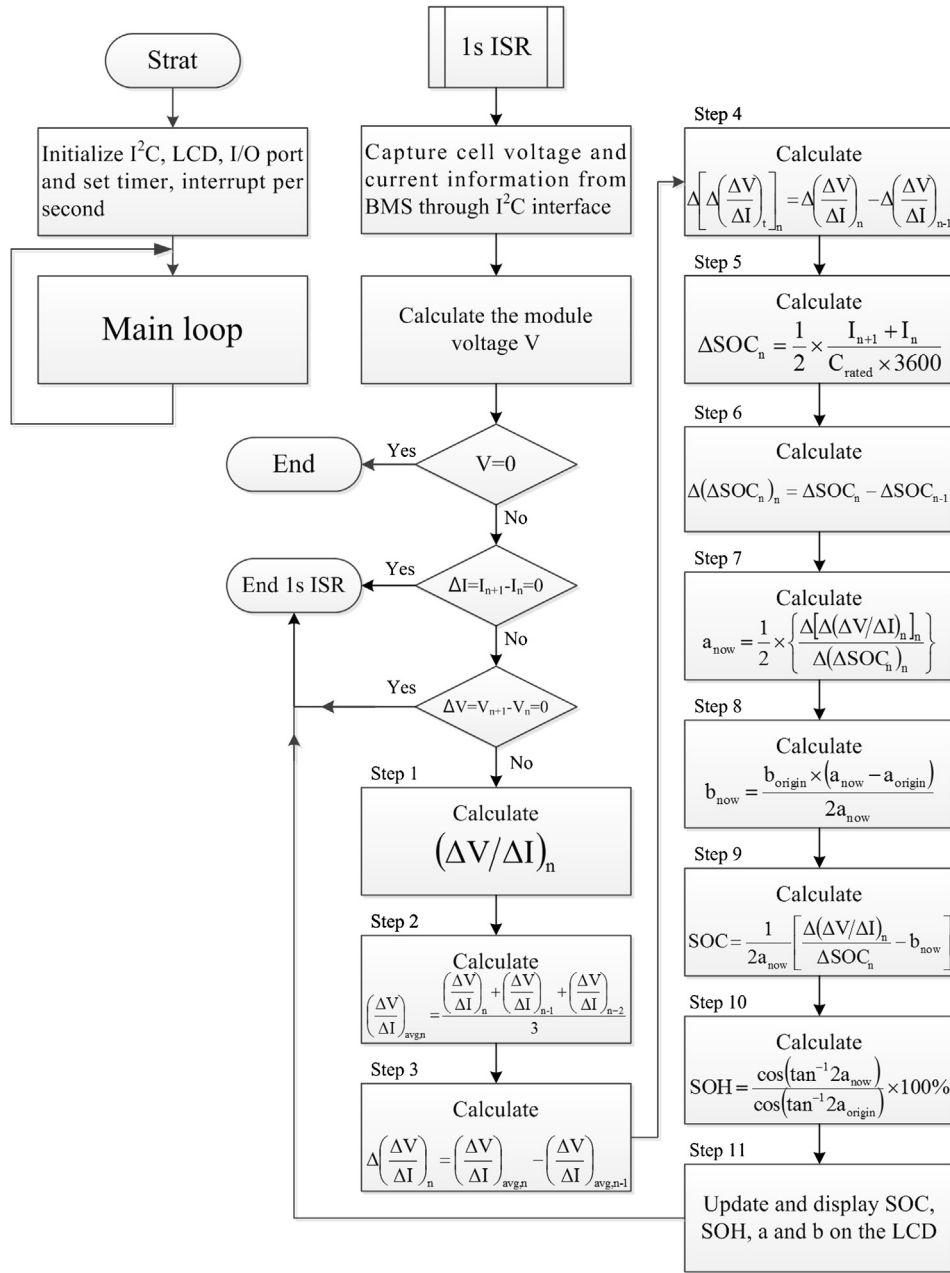


Fig. 15. Flowchart of proposed SOC and SOH estimation method.

simulating the load variations that tend to occur in electric vehicles as a result of variations in road and traffic conditions. As the voltage and current in the battery module changed, we calculated the dynamic impedance and thereby observed the relationship between dynamic impedance and SOC in the module.

Fig. 17 presents the relationship between dynamic impedance and the SOC calculated using experimental-derived data using a new battery. In accordance with theoretical predictions, the relationship between dynamic impedance and the SOC presented a parabolic curve; the red curve represents the trend line. When the SOC of the battery was close to 100% or 0%, the magnitude of dynamic impedance increased. In contrast, the dynamic impedance was lowest when the SOC is approximately 50%. As shown in Fig. 17, dynamic impedance and the SOC present a quadratic relationship, and for this reason, each value for dynamic impedance corresponds

to two values for SOC. In order to determine a single value for SOC, we calculated the rate of change in the dynamic impedance with respect to the SOC, converting the quadratic parabola into an injection. As shown in Fig. 18, this resulted in a single SOC solution for each $\Delta(\Delta V/\Delta I)/\Delta SOC$ value.

We obtained the averages of dynamic impedance to reduce calculation errors, make the curve smoother, and prevent unreasonable SOC values due to dramatic changes in the dynamic impedance. Fig. 19 presents the relationship between dynamic impedance and SOC averaging three consecutive points for dynamic impedance. As can be seen, the trend of the curves did not change from that presented in Fig. 17; however, the changes are smoother and can thus reduce the chance of misjudgment.

After calculating the rate of change in the average dynamic impedance with respect to SOC in Fig. 19, we derive the injection of

Table 2
Specifications of ICR18650-22P lithium-ion battery.

Cathode	Lithium ion NCA (active material) Polyvinylidene fluoride (binder) Carbon black (conductive material)
Anode	Graphite (active material) Polyvinylidene fluoride (binder)
Electrolyte	Organic solvents, lithium salt
Rated capacity	2150 mAh
Maximum discharge current	10 A (4.65 C)
Rated voltage	3.62 V
Maximum voltage	4.2 V
Maximum charge current	2.15 A (1 C)
Cut-off voltage	2.75 V
Cell weight	44.5 g (max)
Cell dimension	Diameter: 18.4 mm (max) Height: 65 mm (max)

$\Delta(\Delta V/\Delta I)/\Delta SOC$ with respect to SOC. To ensure that the results calculated from the average values did not deviate significantly from the original data, we compared the two injections, as shown in Fig. 20. As can be seen, the two curves are nearly identical, with an error small enough to be considered negligible. These experimental results verify the efficacy of the dynamic impedance method proposed in this study in obtaining the SOC of batteries.

Next, to verify the proposed projection technique, we used the battery tester to charge and discharge another battery module at high currents for long time. The purpose was to age the battery before conducting the same experiment. Fig. 21 exhibits the relationship between dynamic impedance and SOC after the battery has been aged. As can be seen, the trend in dynamic impedance is similar to that of a new battery; the magnitude of dynamic impedance is greater when the SOC is near 100% or 0% and smaller near 50%. Once again dynamic impedance presents a quadratic parabola. However, compared with the new batteries, the dynamic impedance is far greater.

To clearly delineate the differences between new and aged batteries, we compared the dynamic impedance and SOC relationship curves of batteries with three different degrees of aging (Fig. 22). As can be seen, the dynamic impedance of the aged batteries is significantly greater than that of the new battery, and the magnitudes of change in the SOC are greater as well.

After calculating the rate of change in the SOC using the curves in Fig. 22, we obtained the relationship between $\Delta(\Delta V/\Delta I)/\Delta SOC$

Table 3
Experiment procedure.

Sequence	Current	Continuous time
1	8.60 A (4 C)	1 s
2	2.15 A (1 C)	1 s
3	4.30 A (2 C)	1 s
4	8.60 A (4 C)	1 s
5	4.30 A (2 C)	1 s
6	2.15 A (1 C)	1 s
7	8.60 A (4 C)	1 s
8	2.15 A (1 C)	1 s

and SOC (Fig. 23). It is clear that the slopes of the curves for the aged batteries are greater and their projections on the SOC axis are shorter, compared to new batteries. In other words, the available capacity of the aged batteries is smaller. As shown in Fig. 23, the available capacities of the two aged batteries were only 84.83% and 89.1% of the rated capacity, whereas the available capacity of the new battery was 93.9% of the rated capacity. This verifies the accuracy of the proposed projection method.

Fig. 24 presents the proposed real-time SOC and SOH estimation system, which includes the BMS, the MCU, and an LCD. As shown in Fig. 24(a), the real-time estimation system comprises two tiers, each containing one of the two major portions of the system: the lower tier contains the BMS, which collects data from the battery module and initiates the protective functions, and the upper tier contains the MCU, which calculates the SOC and the SOH as well as the LCD, which displays the results. The two portions are connected by an I^2C interface. Fig. 24(b) and (c) display the BMS, MCU, and LCD of the proposed system. The BMS includes the detection circuit, which measures the voltage of each cell in the battery module and the charge and discharge currents, the protection circuit for OV, UV, OC, SC, OT, and UT, and two independent charge and discharge loops. The MCU on the upper tier receives data from the battery module via the I^2C interface and calculates the SOC, SOH, and parameters a and b of the battery. The results are updated on the LCD every five seconds.

We used the battery tester to check the accuracy of the developed real-time SOC and SOH estimation system. Using the standard charge and discharge method, we discharged the battery completely. We then adjusted the SOC of the battery from 100% to 0% and employed the proposed estimation technique to calculate the SOC. The proposed system was able to finish calculating the SOC and SOH of the battery in approximately ten seconds. The two curves in Fig. 25 show the SOC set by the battery tester and the SOC results calculated using the proposed estimation system. As

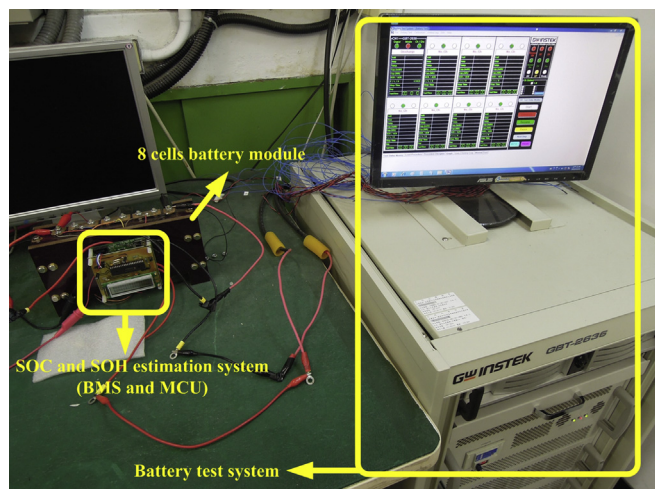


Fig. 16. SOC and SOH estimation experiment.

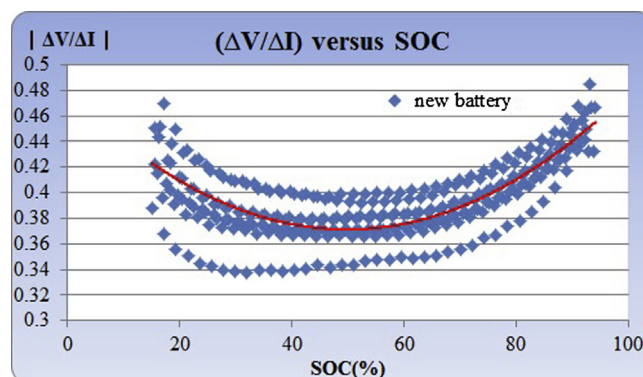


Fig. 17. Relationship between dynamic impedance and SOC in a new battery.

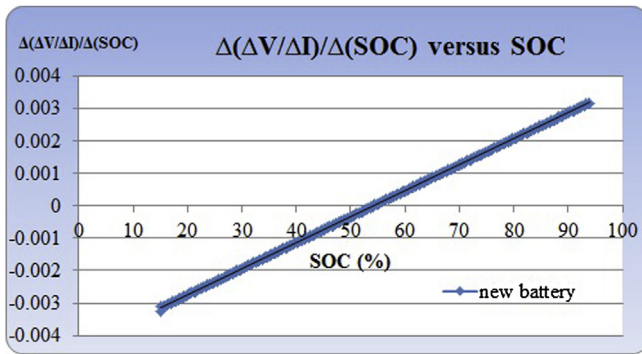


Fig. 18. Relationship between $\Delta(\Delta V/\Delta I)/\Delta SOC$ and SOC in a new battery.

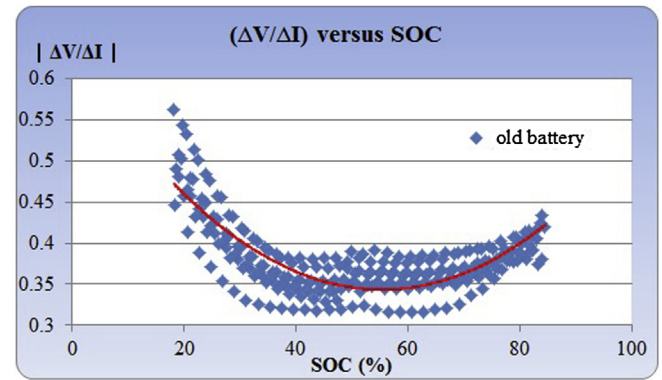


Fig. 21. Relationship between dynamic impedance and SOC in aged battery.

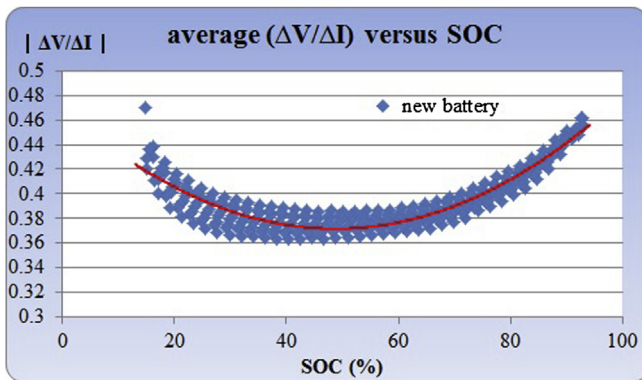


Fig. 19. Relationship between averaged dynamic impedance and SOC in new battery.

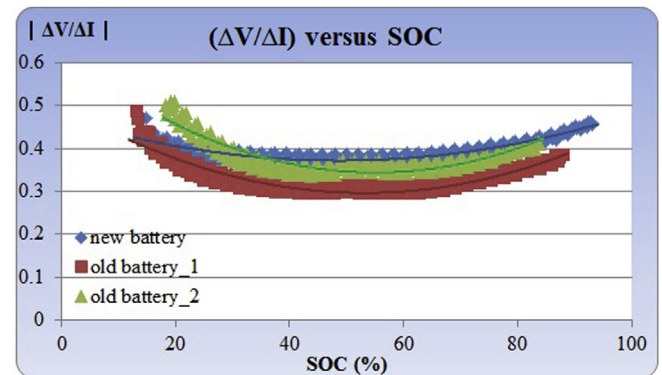


Fig. 22. Comparison of dynamic impedance and SOC in new and aged batteries.

can be seen, the calculated results are consistent with the actual SOC, presenting error of less than 5%. This confirms the accuracy of the developed estimation system and its applicability in real-time detection.

6. Conclusion

This study proposes novel SOC and SOH estimation techniques for lithium-ion batteries. For the estimation of SOC, we define changes in voltage over changes in current during charging and discharging processes as dynamic impedance. For the estimation of SOH, a projection method derives the SOH according to the rate of change in dynamic impedance with respect to SOC. One advantage of these techniques is that they do not require initial values but rather measure the dynamic changes in the battery module during

the charging or discharging processes. Simple operations are then performed to calculate various parameters and provide real-time results. In addition to using dynamic impedance to determine the corresponding relationship between the SOC and the SOH, this study also derived a mathematical model using parameters obtained by capturing the dynamic changes in the battery module. Theoretical deductions and experimental results demonstrate that changes in aging of the battery module are reflected in the dynamic characteristics, thereby automatically updating the parameters used for mathematical modeling. In other words, the SOC is closely linked to the SOH. To verify the accuracy of the proposed estimation methods, we developed a complete SOC and SOH estimation system combining an MCU with BMS without the need for additional testing circuits. The BMS retrieves the voltage and current data, and the MCU executes the estimation methods, thereby achieving real-

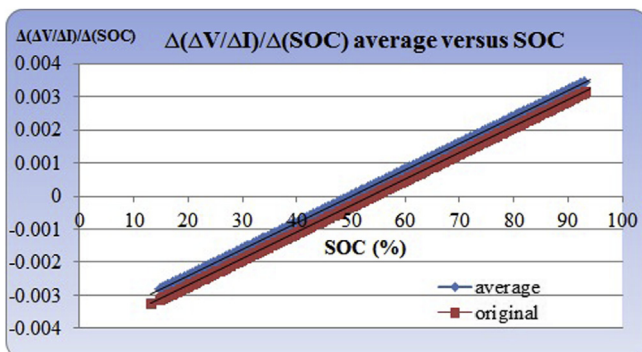


Fig. 20. Comparison between averages of $\Delta(\Delta V/\Delta I)/\Delta SOC$ and SOC in new battery.

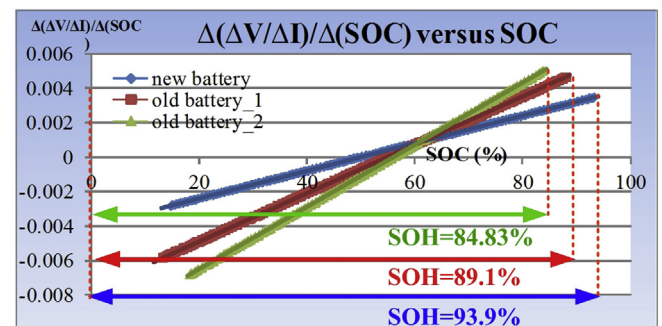
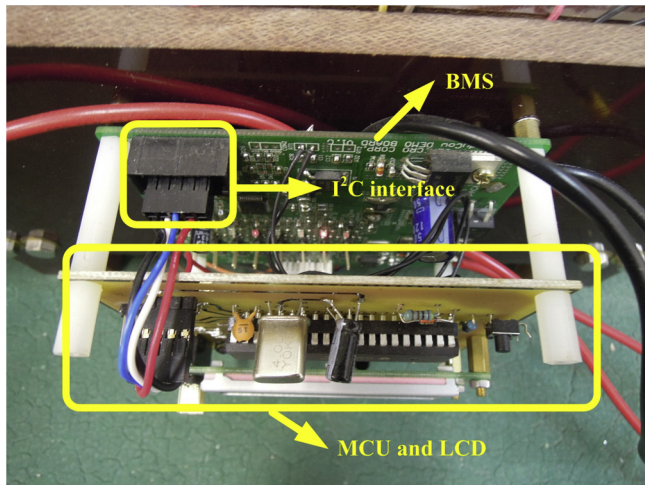
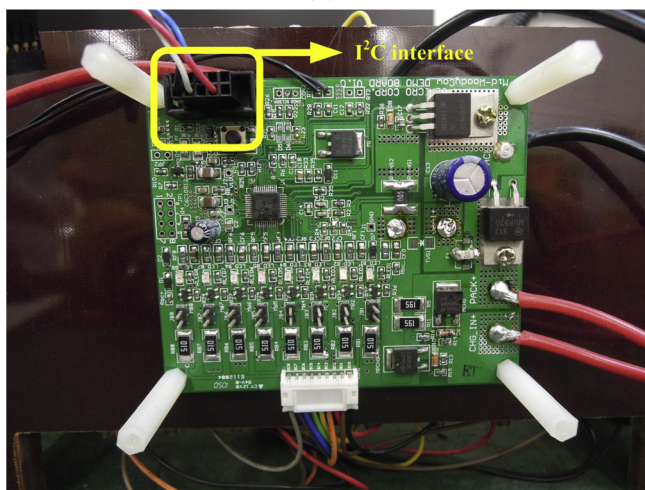


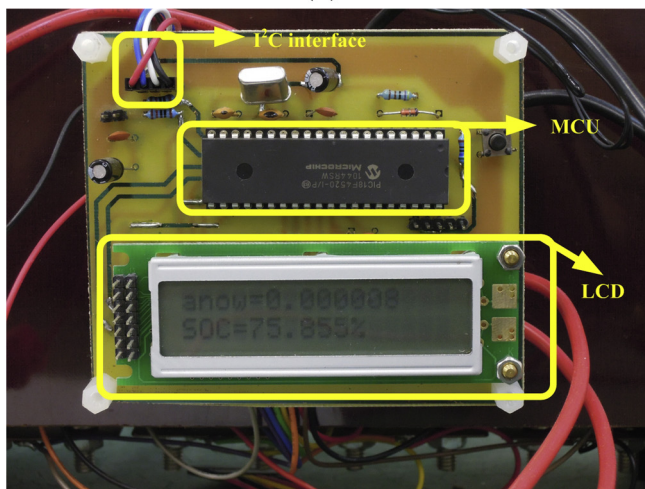
Fig. 23. Comparison of $\Delta(\Delta V/\Delta I)/\Delta SOC$ and SOC in new and aged batteries.



(a)



(b)



(c)

Fig. 24. Proposed real-time SOC and SOH estimation system: (a) overall system, (b) BMS and (c) MCU and LCD.

time estimation. Experiments results confirm that the estimated results are extremely close to actual values. Errors between the estimation results and actual SOC values were less than 5% within a test range from 100% to 0%.

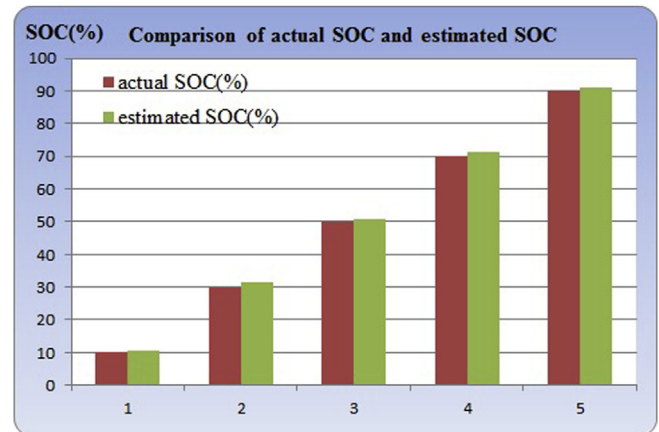


Fig. 25. Comparison of the actual SOC and estimated SOC.

Acknowledgment

This work was sponsored by the National Science Council, Taiwan, R.O.C., Project number: NSC 102-2221-E-036-009-MY2. The authors would also like to thank the Tatung University for their financial support, Project number: B101-E01-027.

References

- [1] J. Remmlinger, M. Buchholz, M. Meiler, P. Bernreuter, K. Dietmayer, *J. Power Sources* 196 (2011) 5357–5363.
- [2] S. Gerssen-Gondelach, A. Faaij, *J. Power Sources* 212 (2012) 111–129.
- [3] L. Lu, X. Han, J. Li, J. Hua, M. Ouyang, *J. Power Sources* 226 (2013) 272–288.
- [4] R. Xiong, F. Sun, X. Gong, H. He, J. Power Sources 242 (2013) 699–713.
- [5] R. Adany, D. Aurbach, S. Kraus, *J. Power Sources* 231 (2013) 50–59.
- [6] H. Fathabadi, *J. Power Sources* 245 (2014) 495–500.
- [7] J. Hooper, J. Marco, *J. Power Sources* 245 (2014) 510–519.
- [8] W. Waag, C. Fleischer, D. Sauer, *J. Power Sources* 258 (2014) 321–339.
- [9] S. Rezvanizani, Z. Liu, Y. Chen, J. Lee, *J. Power Sources* 256 (2014) 110–124.
- [10] S. Bauer, A. Suchanek, F. León, *J. Power Sources* 246 (2014) 808–818.
- [11] T. Tsujikawa, K. Yabuta, M. Arakawa, K. Hayashi, *J. Power Sources* 244 (2013) 11–16.
- [12] X. Han, M. Ouyang, L. Lu, J. Li, Y. Zheng, Z. Li, *J. Power Sources* 251 (2014) 38–54.
- [13] A. Eddahech, O. Briat, J. Vinassa, *J. Power Sources* 258 (2014) 218–227.
- [14] J. Sabatier, M. Merveillaut, J. Francisco, F. Guillemard, D. Porcelatto, *J. Power Sources* 262 (2014) 36–43.
- [15] E. Ferg, C. Rossouw, P. Loyson, *J. Power Sources* 226 (2013) 299–305.
- [16] F. Leng, C. Tan, R. Yazami, M. Le, *J. Power Sources* 255 (2014) 423–430.
- [17] B. Xiong, J. Zhao, Z. Wei, M. Skyllas-Kazacos, *J. Power Sources* 262 (2014) 50–61.
- [18] J. Li, J. Barillas, C. Guenther, M. Danzer, *J. Power Sources* 247 (2014) 156–162.
- [19] L. Maharjan, S. Inoue, H. Akagi, J. Asakura, *IEEE Trans. Power Electron.* 24 (2009) 1628–1636.
- [20] G. Plett, *J. Power Sources* 134 (2004) 252–261.
- [21] G. Plett, *J. Power Sources* 134 (2004) 262–276.
- [22] G. Plett, *J. Power Sources* 134 (2004) 277–292.
- [23] Z. Chen, C. Mi, Y. Fu, J. Xu, X. Gong, *J. Power Sources* 240 (2013) 184–192.
- [24] M. Khan, G. Mulder, J. Mierlo, *J. Power Sources* 246 (2014) 629–641.
- [25] C. Fleischer, W. Waag, H. Heyn, D. Sauer, *J. Power Sources* 260 (2014) 276–291.
- [26] C. Fleischer, W. Waag, H. Heyn, D. Sauer, *J. Power Sources* 262 (2014) 457–482.
- [27] B. Pattipati, C. Sankavaram, K.-R. Pattipati, *IEEE Trans. Syst. Man, Cybernetics – Part C: Appl. Rev.* 41 (2011) 869–884.
- [28] Y. Chiang, W. Sean, J. Ke, *J. Power Sources* 196 (2011) 3921–3932.
- [29] C. Weng, J. Sun, H. Peng, *J. Power Sources* 258 (2014) 228–237.
- [30] X. Hua, S. Li, H. Peng, F. Sun, *J. Power Sources* 217 (2012) 209–219.
- [31] M. Mastali, J. Vazquez-Arenas, R. Fraser, M. Fowler, S. Afshar, M. Stevens, *J. Power Sources* 239 (2013) 294–307.
- [32] D. Andre, C. Appel, T. Soczka-Guth, D. Sauer, *J. Power Sources* 224 (2013) 20–27.
- [33] X. Feng, J. Li, M. Ouyang, L. Lu, J. Li, X. He, *J. Power Sources* 232 (2013) 209–218.
- [34] M. Coleman, W.-G. Hurley, C.-K. Lee, *IEEE Trans. Energy Convers.* 23 (2008) 708–713.

- [35] A. Barré, B. Deguilhem, S. Grolleau, M. Gérard, F. Suard, D. Riu, J. Power Sources 241 (2013) 680–689.
- [36] J. Remmlinger, M. Buchholz, T. Soczka-Guth, K. Dietmayer, J. Power Sources 239 (2013) 689–695.
- [37] D. Andrea, M. Meilera, K. Steinera, C. Wimmera, T. Soczka-Gutha, D. Sauerb, J. Power Sources 196 (2011) 5334–5341.
- [38] D. Andrea, M. Meilera, K. Steinera, H. Walza, T. Soczka-Gutha, D. Sauerb, J. Power Sources 196 (2011) 5349–5356.
- [39] T. Osakaa, T. Momma, D. Mukoyama, H. Nara, J. Power Sources 205 (2012) 483–486.
- [40] L. Raijmakers, D. Danilov, J. Lammeren, M. Lammers, P. Notten, J. Power Sources 247 (2014) 539–544.
- [41] O₂ Micro Datasheet: OZ8920, O₂ Micro International, Ltd., 2009, p. 1.
- [42] O₂ Micro Application Note: 7, O₂ Micro International, Ltd., 2008, pp. 1–8.
- [43] Samsung SDI Product Safety Datasheet, Samsung SDI, 2010, pp. 1–2.